

Optimizing Structural, Optical, Dielectric, and Magnetic Properties of $(\text{Bi}_{1-x}\text{La}_x)\text{FeO}_3$ ($0.00 \leq x \leq 0.06$) Sintered Ceramics

Abid Zaman,* Asad Ali,* Muhammad Anas, Muhammad Kamran, Amir Sohail Khan, Vineet Tirth, Jehan Y. Al-Humaidi, Amir Arabi, Moamen S. Refat, and Rafi Ullah



Cite This: *ACS Omega* 2023, 8, 13222–13231



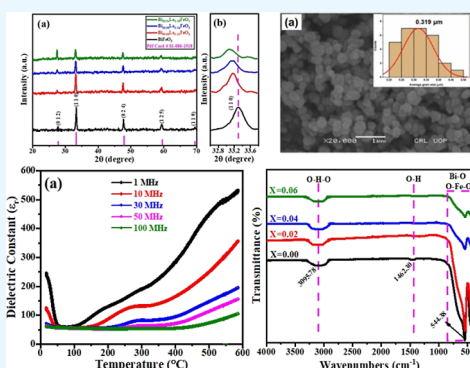
Read Online

ACCESS |

 Metrics & More

 Article Recommendations

ABSTRACT: $(\text{Bi}_{1-x}\text{La}_x)\text{FeO}_3$ ($0.00 \leq x \leq 0.06$) ceramics have been synthesized through a mixed oxide route to investigate their structural, morphological, optical, dielectric, and magnetic properties. All the samples are revealed to be in rhombohedral structures along with the $R\bar{3}c$ space group and 161 space group number. A high relative permittivity and the lowest tangent loss are observed in BLFO samples at the frequency range 1–100 MHz. The optical studies show that the excitation energy increases with the increasing La content. Moreover, the magnetization being strongly affected by crystallite size and microstrain has been investigated. The band gap energy increases with the increasing La content. The overall result of pure and doped La contents in BFO ceramics shows enhanced structural, dielectric, and optical properties.



INTRODUCTION

The renowned perovskite oxide that shows both optical and dielectric properties at room temperature is bismuth ferrite [BiFeO_3 (BFO)]. BFO is one of the single-phase multiferroic materials that exhibit the coexistence of ferroelectric ordering with a Curie temperature (T_C) of 850 °C and antiferromagnetic (AFM) ordering with a Neel temperature (T_N) of 370 °C. The bulk BFO has a rhombohedral structure along with the space group $R\bar{3}C$ at room temperature.¹ The magnetoelectric effect (ME) has been observed in BFO ceramics by switching electric magnetization and polarization mutually.² It is considered that BFO ceramics are a candidate material for many applications i.e., data storage devices, spintronics, transducers, and electromagnetic devices.^{3–5} However, synthesis of BFO (single phase) is very difficult to perform due to (i) current leakage in samples arising due to impurity contents; (ii) formation of a thin thermal window; and (iii) oxygen vacancies and improper stoichiometric ratios.^{6–8} Furthermore, the AFM behavior in BFO ceramics is the main obstacle in obtaining a larger ME effect and hence avoiding its current leakage. The doping procedure and modified synthesis method of BFO ceramics help a certain amount in restraining the aforesaid impairments. The total magnetization in BFO is initiated from the spin phase of the Fe^{3+} cation, while the total polarization may result from the stereochemical approach of $6s^2$ single pair electrons in the Bi^{3+} cation.^{9–12} The multiple sample properties would be modified by the help of doping elements. There are many reports that expressed one-site doping at either the A or B site cation.^{13–16} The doping of La

or Ba will improve the dielectric properties and minimize the current leakage, while the doping of Mn and Ti ions will improve optical and magnetic properties.^{17–22} However, the A site cation doping not only produces strain in the sample but also added to the magnetic contributions. Besides these, there have been some reports in this regard to investigate the multiple properties. For example, the doping of V^{5+} and La^{3+} in the BFO sample enhanced the structural, microstructural, optical, and dielectric properties,^{23–26} while very few reports show the modified magnetic properties in the framework.^{27–29} Many researchers reported that the phase transition and miniaturization of leaking currents also occur in the BFO sample due to doping of (La, Pr) and (La, Sm), which further stabilizes the magnetic properties.^{30,34} The rare-earth metals, e.g., Gd, play a key role in increasing the magnetization behaviors.^{35,36} It is very interesting to studies the effect of A-site doping of La or Gd cations, which may affect the optical, dielectric, and magnetic properties.^{32,33}

In the present study, an effort is made to synthesize the $(\text{Bi}_{1-x}\text{La}_x)\text{FeO}_3$ sintered ceramics ($0.00 \leq x \leq 0.06$) via a solid-state route. In this method, the ball milling is a mechanical technique that is broadly used to grind powders

Received: January 24, 2023

Accepted: March 16, 2023

Published: March 27, 2023



ACS Publications

© 2023 The Authors. Published by
American Chemical Society

into fine particles, and its effect on the crystallite size, dielectric properties, and microstructure development of milled powders is studied. Due to this importance, we studied the effect of La^{3+} on the relationship between the structural, microstructural, vibrational, and dielectric properties (dielectric constant and tangent loss) of the $(\text{Bi}_{1-x}\text{La}_x)\text{FeO}_3$ materials, which by varying the frequency as well as temperature are improved.

RESULTS AND DISCUSSION

Phase Analysis. Figure 1b represents the X-ray diffraction (XRD) pattern of La-doped BiFeO₃ sintered ceramics obtained

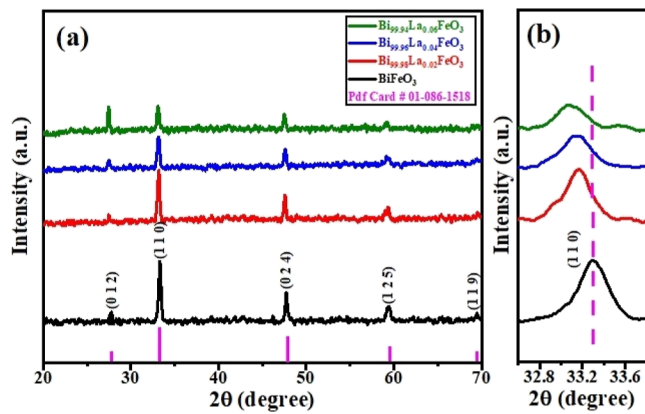


Figure 1. (a) XRD pattern of La doped in BiFeO_3 sintered at 800 °C for 30 min. (b) Enlarged view of the shift of the lower 2θ peak at (1 1 0).

for structural information. All major peaks are indexed properly (base sample only) and show a rhombohedral structure along with the lattice parameters ($a = b = c = 0.5620 \text{ nm}$) and space group ($R\bar{3}c$) that matched with JCPDs no. 01-086-1518. A minuscule amount of the secondary phase of $\text{Bi}_{25}\text{FeO}_{40}$ and $\text{Bi}_2\text{Fe}_4\text{O}_9$, along with the primary phase is observed for BFO ceramics.³⁷ The major diffracted peak (1 1 0) is shifted to lower 2θ values with increasing La contents, as shown in Figure 1b. The shifting of the major peak to a lower Bragg's angle is due to the variation in the ionic radii of Bi^{3+} (1.17 Å) and La^{3+} (1.03 Å).³⁸ The compressive stress (lattice distortion) produced in the La-doped BFO rhombohedral structure is due to the ionic radius difference.

However, the major peak shifting toward lower Bragg's angle shows the induced stress, ascribed to the increasing La concentration. Moreover, no phase transition is detected for all compositions. Densification of the samples mostly affected the microstructural, optical, and dielectric properties. Therefore, the dignified density and relative density of samples have been calculated. Additionally, to correlate the crystallite size with La contents, the average crystallite size is calculated from the full width at half maximum (fwhm) of the all samples by using the Debye–Scherer formula, and it is noted to be decrease with increasing La contents.³⁹

$$D = \frac{k\lambda}{\beta \cos \theta} \quad (1)$$

where "D" is the crystallite size, "k" is the shape factor (~ 0.9), " β " is the fwhm measured in radians, " λ " is the wavelength of Cu K α , and " θ " is the Bragg angle. It was observed that the average crystallite size decreases with increasing La contents due to the smaller ionic radius of the La^{3+} (1.03 Å) ion than

the ionic radius of the Bi^{3+} (1.17 Å) ion.⁴⁰ This result confirms the substitution of the La element in the Bi site inside the host matrix. The lattice strain (η) was obtained by using the following equation⁴¹

$$\eta = \frac{\beta \cos \theta}{4} \quad (2)$$

η is observed to be increase with the La concentration. The microstructure and crystallite size significantly affect the optical, magnetic, and dielectric properties.³¹ The value of relative permittivity and magnetization changed with the increasing La concentration in BFO ceramics. The dislocation density (δ) of the BFO sample is produced by the addition of La dopants. The dislocation density of each peak in the BFO sample was calculated by using the following equation.⁴¹

$$\delta = \frac{1}{D^2} \quad (3)$$

The dislocation density increases with increasing La contents in BFO sintered ceramics, as shown in Table 1.

Table 1. W–H Calculated Crystallite Size (D_{W-H}), Dislocation Density (δ_{W-H}), Lattice Strain (η_{W-H}), and Microstrain (ε_{W-H}) of $\text{Bi}_{1-x}\text{La}_x\text{FeO}_3$ ($0.00 \leq x \leq 0.06$) Ceramics

parameters	$x = 0.00$	$x = 0.02$	$x = 0.04$	$x = 0.06$
average crystallite size " D_{W-H} " (nm)	29.0071	32.1703	27.0281	36.3921
dislocation density " δ_{W-H} " ($\times 10^{-3} \text{ nm}^{-2}$)	1.1880	0.9661	1.3695	0.7553
lattice strain " η_{W-H} " ($\times 10^{-4}$)	4.1536	2.9848	4.7726	8.2746
microstrain " ε_{W-H} " ($\times 10^{-2}$)	1.3375	1.3525	1.4351	1.4573

The microstrain (ε) is the degree of distortion present in the crystalline lattice. Both crystallite size and microstrain in the crystal lattice affected the broadening of the XRD lines. This line broadening can be used to measure both the crystallite size and microstrain, and it can be calculated by using the following equation.⁴²

$$\varepsilon = \frac{1}{4 \tan \theta} \quad (4)$$

The Williamson Hall (W–H plot) method can be used to analyze the broadening of peaks.³⁹

$$\beta \cos \theta \frac{k\lambda}{D} + 4\varepsilon \sin \theta \quad (5)$$

The above equation represents a straight line, where ε is the slope of the line and $k\lambda/D$ is the y intercept. Now, we plot $4\sin \theta$ on the x-axis and $\beta \cos \theta$ on the y-axis. The value of crystallite size can be obtained from the y intercept. Figure 2a–d shows WH plots for $\text{Bi}_{1-x}\text{La}_x\text{FeO}_3$ ($0.00 \leq x \leq 0.06$) ceramics. The WH plot is used to analyze crystalline shapes and strain that contribute to X-ray line broadening because Scherer's formula does not take into account the strain contribution. Therefore, the crystallite size, dislocation density, and strain of the W–H plot for $\text{Bi}_{1-x}\text{La}_x\text{FeO}_3$ ($0.00 \leq x \leq 0.06$) ceramics are obtained, as shown in Table 1.

Microstructural Studies. Figure 3 shows the microstructural studies of the thermally etched and gold-coated samples of $\text{Bi}_{1-x}\text{La}_x\text{FeO}_3$ ($0.00 \leq x \leq 0.06$) sintered ceramics.

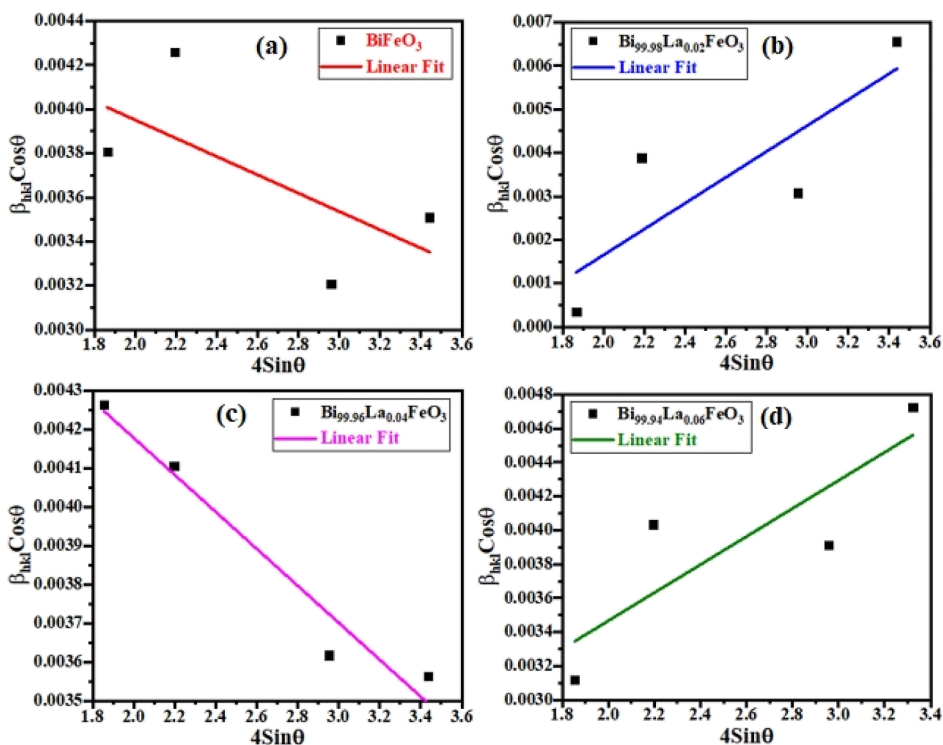


Figure 2. W–H plot of $\text{Bi}_{1-x}\text{La}_x\text{FeO}_3$ ($0.00 \leq x \leq 0.06$) sintered ceramics: (a) BiFeO_3 , (b) $\text{Bi}_{99.98}\text{La}_{0.02}\text{FeO}_3$, (c) $\text{Bi}_{99.96}\text{La}_{0.04}\text{FeO}_3$, and (d) $\text{Bi}_{99.94}\text{La}_{0.06}\text{FeO}_3$.

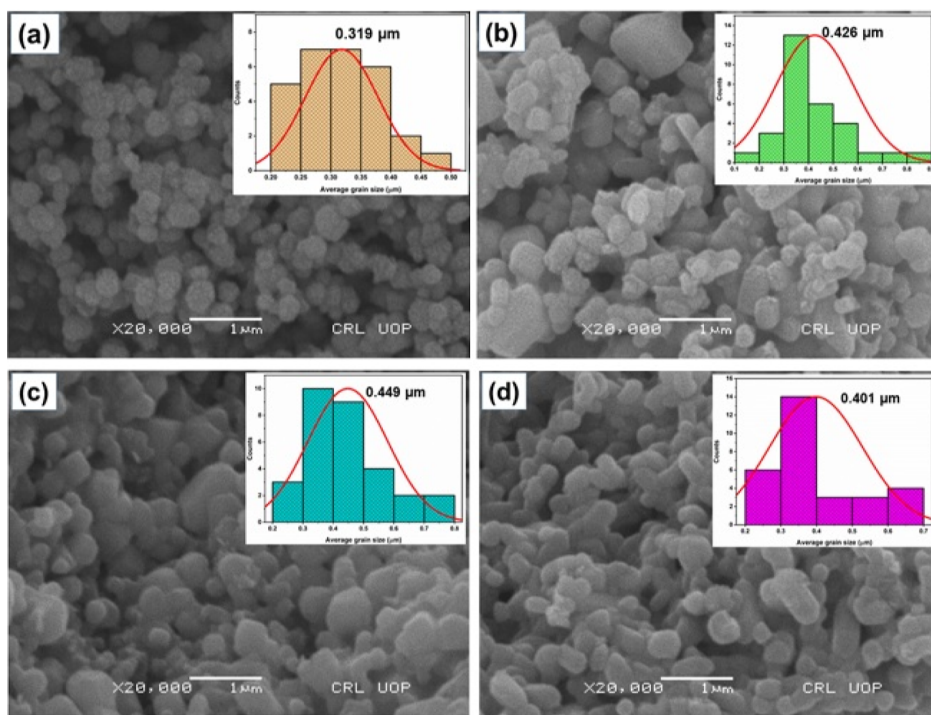


Figure 3. SEM images of $\text{Bi}_{1-x}\text{La}_x\text{FeO}_3$ ($0.00 \leq x \leq 0.06$): (a) $x = 0.00$, (b) $x = 0.02$, (c) $x = 0.04$, and (d) $x = 0.06$.

All the scanning electron microscopy (SEM) images are measured with the same magnification of 20,000 by using a lens detector. The images revealed that all the samples are highly dense, compact, randomly oriented, and non-uniform grains. The average grain or crystallite size has been measured by using ImageJ software. The grain size increases along with La concentration. The reticence of grain growth with

increasing La contents might be attributed to the ionic radius variation of host and substituted atoms. These disparities of ionic radii resulted in the lattice distortion and suppression of grain growth.

Energy-dispersive X-ray spectroscopy (EDX) is used for elemental analysis (quantitative and qualitative) of the samples. Results revealed that a clear peak is present in the spectrum for

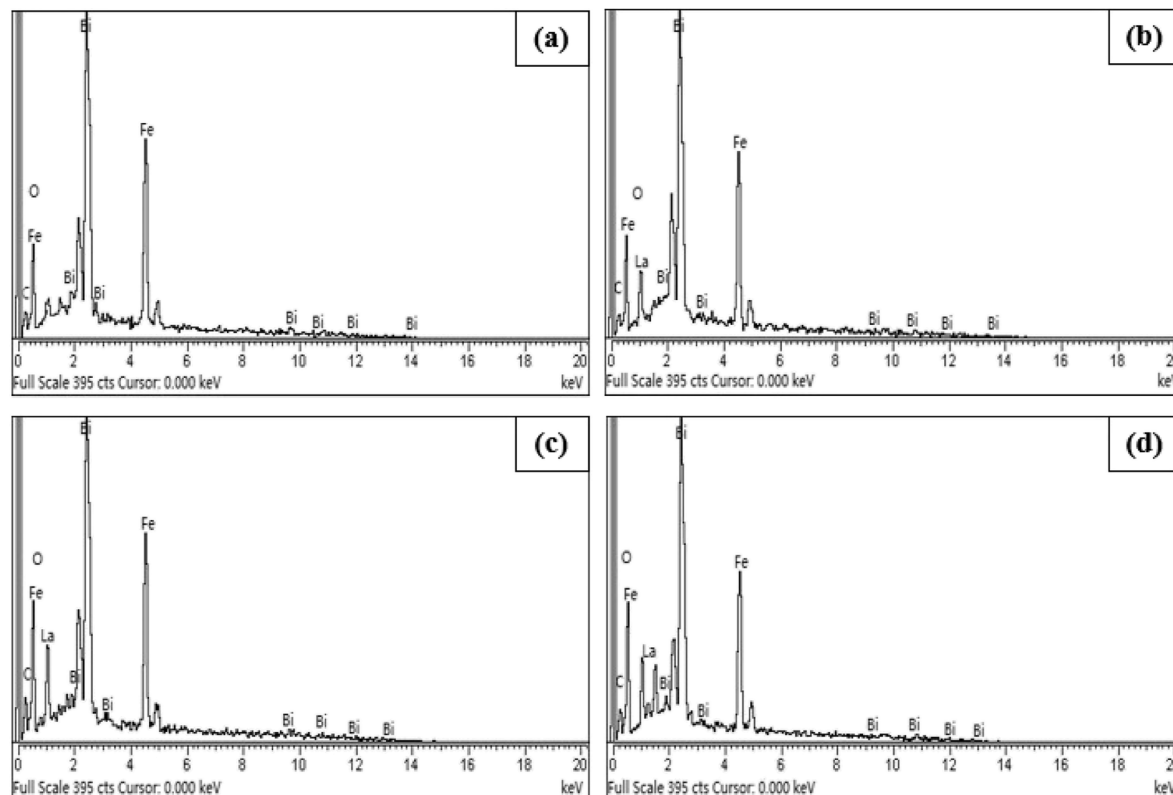


Figure 4. EDX spectra of pure and La-doped BFO ceramics: (a) $x = 0.00$, (b) $x = 0.02$, (c) $x = 0.04$, and (d) $x = 0.06$.

all the elements, which is the evidence of La ions having been doped in the BFO structure successfully, as shown in Figure 4.²⁸ For the purity confirmation of samples, the EDX spectrum is recorded with different weight percentage (wt %) levels on every sample to determine the homogeneity of La absorption in BFO ceramics. Increasing La concentration is characterized by the enlarged intensity of the La peak and a decrease in intensity of Bi peaks. It is revealed that Bi, O, La, and Fe elements are present in the samples, and the ratio of the atomic percentage of elements in the samples matches the stoichiometric ratio with quantity taken for their research. There is no impurity found in pure BFO and La-doped BFO.

Fourier Transform Infrared Spectroscopy. Figure 5 shows the Fourier transform infrared (FTIR) spectra of

$\text{Bi}_{1-x}\text{La}_x\text{FeO}_3$ ($0.00 \leq x \leq 0.06$) sintered ceramics. This analysis is revealed to study the molecular bonding in a ceramic sample. FTIR spectra have some peaks that correspond to vibrational frequency of atomic bonds. This will help classify the bonds present in a material. The peaks at locations 3095.78 and 1462.30 cm^{-1} show symmetric stretching modes of $\text{O}-\text{H}-\text{O}$ and $\text{O}-\text{H}$, respectively, while the peak at location 544.348 cm^{-1} shows the vibrational bending mode of Bi/O and $\text{O}/\text{Fe}/\text{O}$ bonds. In octahedral FeO_6 , vibrations of $\text{Fe}-\text{O}$ show a peak at 520 cm^{-1} . For the out-of-phase vibration, the peak of the oxygen atom perpendicular to plane (111) is observed at 577 cm^{-1} .⁴³ Due to the highest grade of the crystalline phase, pure BFO has an $\text{Fe}-\text{O}$ absorption peak near 600 cm^{-1} . The oxygen bond confirmed the formations of a simple perovskite. The peak below 1000 cm^{-1} wavenumber shows $\text{Bi}-\text{O}$ vibration. Some researchers reported that the peak located near 1000 and 1025 cm^{-1} can be ascribed to the vibration of the $\text{Bi}-\text{O}$ bond.⁴⁴ The grain growth increases with the temperature increase. The vibrational frequency for the $\text{Fe}-\text{O}$ bond is determined by the equation.⁴⁵

$$\nu = \frac{1}{2\pi c} \sqrt{\frac{K}{\mu}} \quad (6)$$

Optical Studies. A UV-visible diffuse reflectance spectrum in the wavelength range of 200 – 800 nm at room temperature is recorded to find the ceramics' optical band gap energy. The optical band gap energy of BFO ceramic arises due to the hybridization of $3d$ and $2p$ orbitals.⁴⁶ The energy band gap of the material can be evaluated using the classical Tau's equation⁴⁷

$$(ah\nu)^n = A(h\nu - E_g) \quad (7)$$

Figure 5. FTIR spectra of $(\text{Bi}_{1-x}\text{La}_x)\text{FeO}_3$ ($0.00 \leq x \leq 0.06$) ceramics.

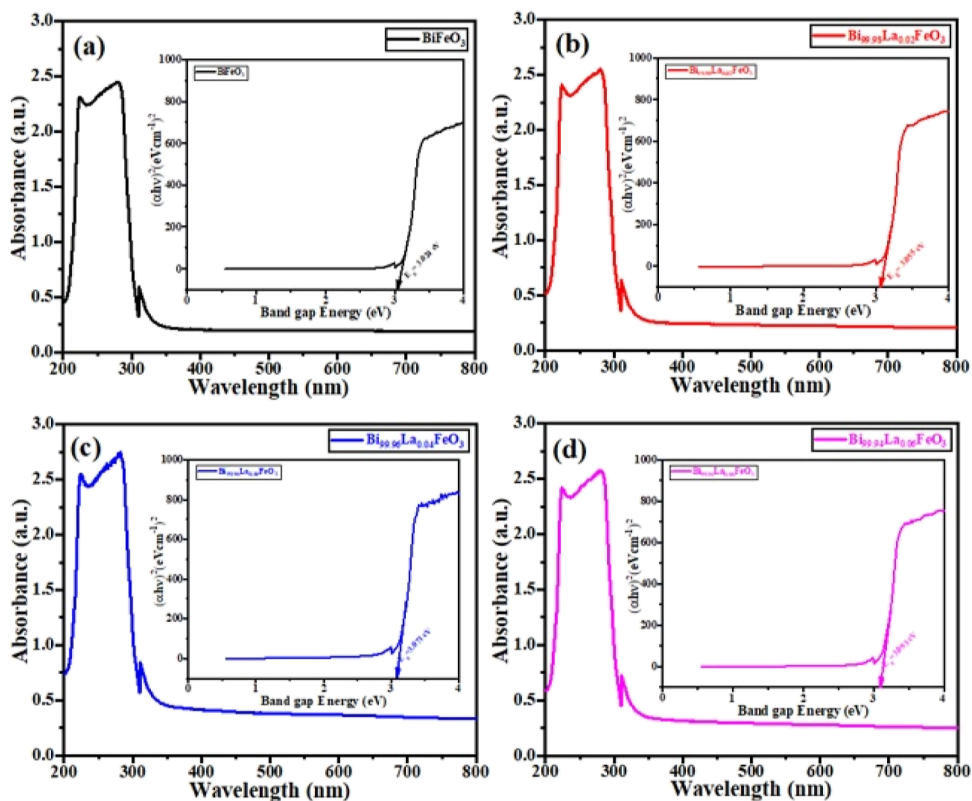


Figure 6. UV spectra of $(\text{Bi}_{1-x}\text{La}_x)\text{FeO}_3$ ($0.00 \leq x \leq 0.06$) sintered ceramics: (a) BiFeO_3 , (b) $\text{Bi}_{99.98}\text{La}_{0.02}\text{FeO}_3$, (c) $\text{Bi}_{99.96}\text{La}_{0.04}\text{FeO}_3$, and (d) $\text{Bi}_{99.94}\text{La}_{0.06}\text{FeO}_3$.

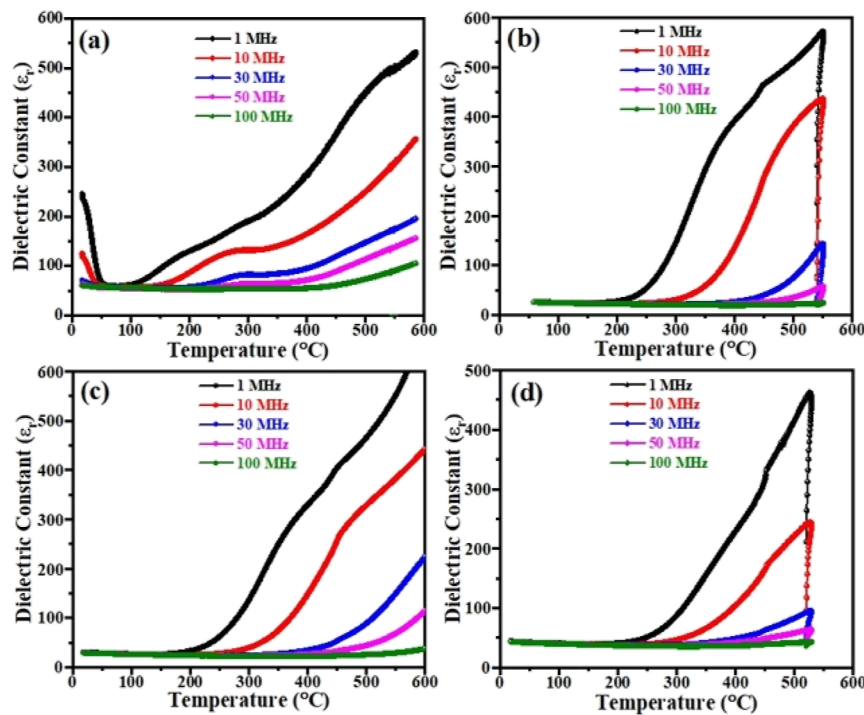


Figure 7. Variation of relative permittivity of BLFO sintered ceramics with temperature: (a) $x = 0.00$, (b) $x = 0.02$, (c) $x = 0.04$, and (d) $x = 0.06$.

where A is a constant, $h\nu$ is the photon energy, α is the adsorption coefficient, E_g denotes the band gap, and n is a number having values 2 and $1/2$. The value of n depends on electronic transitions: $n = 1$ for direct band gap energy and $n = 1/2$ for indirect band gap energy.^{48–51} Figure 6a–d represents

the Tauc plots in $(\alpha h\nu)^2$ versus photon energy for all ceramics. The direct band gap of the samples was extracted by linear extrapolation of $(\alpha h\nu)^2$ versus energy (E) plots to zero. The optical band gaps estimated for BFO, $x = 0.02$, $x = 0.04$, and $x = 0.06$ are 3.024, 3.055, 3.071, and 3.093 eV, respectively. The

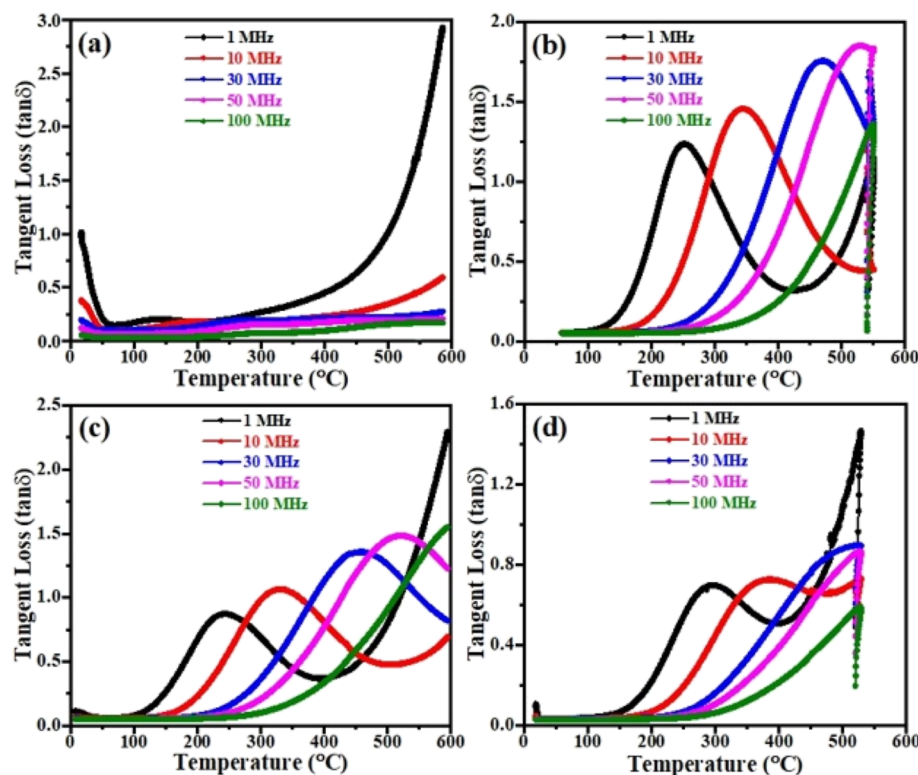


Figure 8. Variation of tangent loss of BLFO sintered ceramics with temperature: (a) $x = 0.00$, (b) $x = 0.02$, (c) $x = 0.04$, and (d) $x = 0.06$.

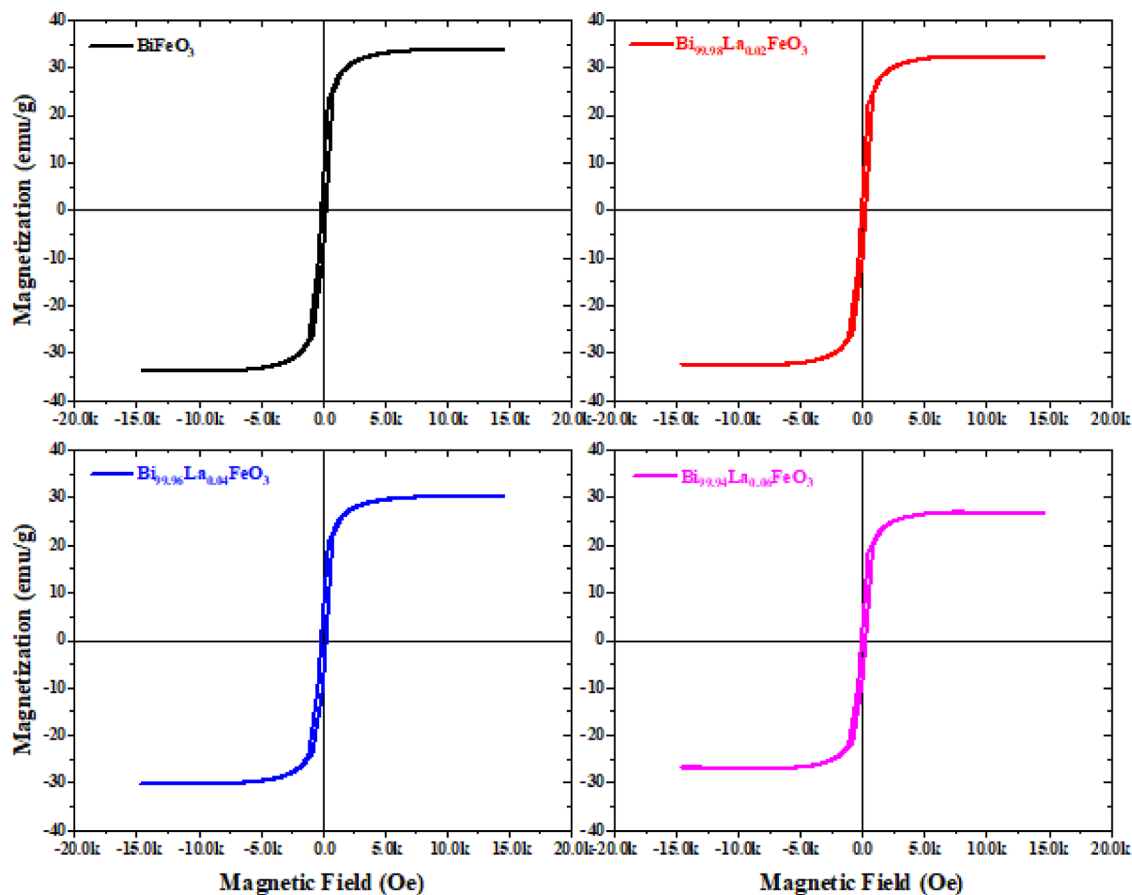


Figure 9. Variation of magnetization of BLFO sintered ceramics with magnetic field.

band gap energy increases with La contents, which may be due to the distortion of the lattice system. Therefore, we observe tremendous optical properties compared to that of conventional ferroelectric materials, which show large band gap energies of 3.024–3.095 eV and BFO-based materials show a band gap less than 2.734 eV.^{52,53}

Dielectric Properties. Figure 7 shows the relative permittivity or dielectric constant (ϵ_r) and tangent loss or dielectric loss ($\tan \delta$) measured for $(\text{Bi}_{1-x}\text{La}_x)\text{FeO}_3$ ($0.00 \leq x \leq 0.06$) sintered ceramics at the 1–100 MHz frequency range. It is reported that the value of ϵ_r increases with La contents and decreases with frequency. The lowest value of tangent loss ($\tan \delta$) is obtained for the highest doping of La, i.e., at content ($x = 0.06$), as shown in Figure 8. It has been reported that the $\tan \delta$ decreases with La contents while the value of relative permittivity is maintained.⁵⁴ The particular mechanism for the decrease in tangent loss value with the increasing La content has not been understood. However, it can be recommended that La ions help in (a) the stability of the BFO structure, (b) reducing Bi losses, and (c) increasing the material density. This indicated that the valence state of iron (Fe^{3+}) arose due to the loss of Bi with the substitution of La^{3+} by Bi^{3+} . So, reducing the electronic springing from the Fe^{3+} ion to Fe^{2+} arising due to ion disproportionality between the off stoichiometric ratios of Bi^{3+} and Fe^{3+} ions reduces the secondary phase formation, which contributed in the conduction of pure BFO.⁵⁵ This doping weakens the conductivity, which reduces the tangent loss. Lastly, increasing density also participated in reducing the tangent loss.

In pure BFO, the polar activities of the Bi cation are the main cause for the remark of space charge polarization. In this study, the recorded relative permittivity is not only due to Bi ion but also the geometry of the crystal, which results in the doping-based dielectric properties. The value of ϵ_r is improved by La doping and crystal distortion as well. The distortion may result in the different bond lengths in $\text{Fe}-\text{O}$, which lead to the development of polarization and ϵ_r through off-centrosymmetry. The reducing secondary phases from the BLFO ceramics contributed in enhancing ϵ_r by avoiding the conduction of electrons from the secondary phase. Additionally, the doping of La^{3+} ion enables the reimbursement of oxygen vacancies, and even the energy of bond separation (for the $\text{La}-\text{O}$ bond) is greater than that for the $\text{Bi}-\text{O}$ bond.⁵⁶ The BLFO with different contents shows the low $\tan \delta$ and the highest ϵ_r , which shows that the La^{3+} ion improves the optical, dielectric, and magnetic properties effectively for practical applications.

Magnetic Properties. Figure 9 shows the magnetic properties of BLFO sintered ceramics at room temperature. All of the samples show hysteretic behavior with linear components, features of an AFM material, in accordance with that reported for BLFO samples.⁵⁷ When compared to the results for the sample of pure BFO found by Dias et al., an increasing magnetization is observed.⁵⁸ The substitution of La maybe affects the magnetic properties, which further produces distortion in the unit cell due to the difference in ionic radii of host and dopant atoms. In BLFO samples, the magnetization is influenced by the $\text{Fe}-\text{O}-\text{Fe}$ bond distortions. So, the observed variations in magnetization for BLFO samples are affected by the chemical strains.⁵⁹ The magnetic properties of BFO are greatly affected by crystallite size, microstrain, doping elements, etc.^{60–62} The presence of microstrain is essential to explain why the variations in magnetization curves also affected

the magnetic properties.⁶³ In fact, magnetization increases with the decreasing crystallite size.

In this work, we have observed similar results for doped BFO samples.⁶⁴ The magnetization increases with the increase in the La contents and the magnetic field as well, as shown in Table 2.

Table 2. Magnetic Parameters of $(\text{Bi}_{1-x}\text{La}_x)\text{FeO}_3$ ($0.00 \leq x \leq 0.06$) Sintered Ceramics at Different Magnetic Fields (1k, 3k, and 5k Oe)

sample compositions	magnetic field (1k Oe), magnetization (emu/g)	magnetic field (3k Oe), magnetization (emu/g)	magnetic field (5k Oe), magnetization (emu/g)
BiFeO_3	27.34	31.65	33.22
$\text{Bi}_{99.98}\text{La}_{0.02}\text{FeO}_3$	25.97	30.86	31.28
$\text{Bi}_{99.96}\text{La}_{0.04}\text{FeO}_3$	23.44	28.54	29.75
$\text{Bi}_{99.94}\text{La}_{0.06}\text{FeO}_3$	21.45	25.39	26.59

CONCLUSIONS

The solid solutions of $(\text{Bi}_{1-x}\text{La}_x)\text{FeO}_3$ ($0.00 \leq x \leq 0.06$) ceramics are prepared by a mixed oxide route. All the samples show rhombohedral structure along with the space group ($R\bar{3}c$), and no phase transition is observed. The FTIR spectra confirmed the perovskite phase and structural distortion in BLFO ceramics. The obtained band gap values are suitable for the application of light harvesting and solar radiations. The optimum value of relative permittivity with a low tangent loss was recorded at content $x = 0.04$. The band gap energy increasing with the increasing La contents is recorded. The magnetization behaviors are strongly affected by the crystallite size and microstrain. The overall obtained results are suitable for practical applications.

EXPERIMENTAL METHOD

The solid solutions of $(\text{Bi}_{1-x}\text{La}_x)\text{FeO}_3$ ($0.00 \leq x \leq 0.06$) ceramics are synthesized by amixed oxide route. Stoichiometric ratios of Fe_2O_3 , Bi_2O_3 and La_2O_3 powders are mixed and milled systematically in an ethanol medium by using horizontal ball milling for 3 h. The zirconia balls of diameters 5 and 10 mm have been used in this experimental work. The slurry (wet mixture of raw powders) was kept in a microwave oven at 90 °C for 24 h to dry it. The dried mixture was re-milled for 1 h to reduce agglomerations. Then, the mixture was calcined at 850 °C for 3 h. Moreover, the pellets were prepared and sintered at 980 °C for 3 h. The phase formation of sintering and milling samples was performed through an X-ray diffractometer (JDX-3532, JEOL, Japan) with $\text{Cu K}\alpha$ radiations of wavelength $\lambda = 0.1540598$ nm, functioning at 45 kV and 40 mA to identify the phases. The samples were analyzed for their surface morphology by using SEM (Carl Zeiss Ultra 55, USA), and EDX analysis was carried out for elemental compositions. To measure dielectric properties, silver was pasted on both sides of the pellet samples to make the geometry of a capacitor. Relative permittivity (ϵ_r) measurements were carried out by using an LCR meter (Agilent E4980A, USA) at room temperature. The magnetic properties of these samples were studied by using a Quantum Design PPMS-VSM in the presence of an external magnetic field, and hysteresis loops were recorded at room temperature.

AUTHOR INFORMATION

Corresponding Authors

Abid Zaman — Department of Physics, Riphah International University, Islamabad 44000, Pakistan;  orcid.org/0000-0001-9527-479X; Email: zaman.abid87@gmail.com

Asad Ali — Department of Physics, Riphah International University, Islamabad 44000, Pakistan; Department of Physics, Government Post Graduate College, Nowshera, Khyber Pakhtunkhwa 24100, Pakistan; Email: kasadiiui@gmail.com

Authors

Muhammad Anas — Department of Physics, Abdul Wali Khan University Mardan, Mardan, Khyber Pakhtunkhwa 23200, Pakistan

Muhammad Kamran — Department of Electronics, University of Peshawar, Peshawar 25120, Pakistan

Amir Sohail Khan — Department of Physics, Islamia College Peshawar, Peshawar, Khyber Pakhtunkhwa 25120, Pakistan

Vineet Tirth — Mechanical Engineering Department, College of Engineering, King Khalid University, Abha, Asir 61421, Kingdom of Saudi Arabia; Research Center for Advanced Materials Science (RCAMS), King Khalid University, Abha, Asir 61413, Kingdom of Saudi Arabia;  orcid.org/0000-0002-8208-7183

Jehan Y. Al-Humaidi — Department of Chemistry, College of Science, Princess Nourah bint Abdulrahman University, Riyadh 11671, Saudi Arabia

Amir Arabi — Mechanical Engineering Department, College of Engineering, King Khalid University, Abha, Asir 61421, Kingdom of Saudi Arabia

Moamen S. Refat — Department of Chemistry, College of Science, Taif University, Taif 21944, Saudi Arabia

Rafi Ullah — Faculty of Materials and Manufacturing, Beijing University of Technology, Beijing 100124, China

Complete contact information is available at:

<https://pubs.acs.org/10.1021/acsomega.3c00495>

Notes

The authors declare no competing financial interest.

ACKNOWLEDGMENTS

The authors extend their appreciation to the Deanship of Scientific Research at King Khalid University Abha 61421, Asir, Kingdom of Saudi Arabia for funding this work through the Small Groups Project under grant number RGP.1/123/43. Princess Nourah bint Abdulrahman University Researchers Supporting Project number (PNURSP2023R24), Princess Nourah bint Abdulrahman University, Riyadh, Saudi Arabia.

REFERENCES

- (1) Zhao, T.; Scholl, A.; Zavaliche, F.; Lee, K.; Barry, M.; Doran, A.; Cruz, M. P.; Chu, Y. H.; Ederer, C.; Spaldin, N. A. Electrical control of antiferromagnetic domains in multiferroic BiFeO₃ films at room temperature. *Nat. Mater.* **2006**, *5*, 823–829.
- (2) Lebeugle, D.; Colson, D.; Forget, A.; Viret, M.; Bataille, A. M.; Gukasov, A. Electric-field-induced spin flop in BiFeO₃ single crystals at room temperature. *Phys. Rev. Lett.* **2008**, *100*, 227602.
- (3) Lu, Y. S.; Dai, J. Q. Enhanced electrical properties of (Zn, Mn)-modified BiFeO₃–BaTiO₃ lead-free ceramics prepared via sol–gel method and two-step sintering. *J. Alloys Compd.* **2022**, *899*, 163387.
- (4) Zhang, F.; Zeng, X.; Bi, D.; Guo, K.; Yao, Y.; Lu, S. Dielectric, ferroelectric, and magnetic properties of Sm-doped BiFeO₃ ceramics prepared by a modified solid-state-reaction method. *Materials* **2018**, *11*, 2208.
- (5) Maleki, H. Characterization and photocatalytic activity of Y-doped BiFeO₃ ceramics prepared by solid-state reaction method. *Adv. Powder Technol.* **2019**, *30*, 2832–2840.
- (6) Karpinsky, D. V.; Silibin, M. V.; Trukhanov, S. V.; Trukhanov, A. V.; Zhaludkevich, A. L.; Latushka, S. I.; Zhaludkevich, D. V.; Khomchenko, V. A.; Alikin, D. O.; Abramov, A. S.; et al. Peculiarities of the crystal structure evolution of BiFeO₃–BaTiO₃ ceramics across structural phase transitions. *Nanomaterials* **2020**, *10*, 801.
- (7) Durga Rao, T.; Asthana, S. Evidence of improved ferroelectric phase stabilization in Nd and Sc co-substituted BiFeO₃. *J. Appl. Phys.* **2014**, *116*, 164102.
- (8) Jangid, S.; Barbar, S. K.; Bala, I.; Roy, M. Structural, thermal, electrical and magnetic properties of pure and 50% La doped BiFeO₃ ceramics. *Phys. B* **2012**, *407*, 3694–3699.
- (9) Kum-onsa, P.; Chanlek, N.; Thongbai, P.; Srepusharawoot, P. Effect of complex defects on the origin of giant dielectric properties of Mg²⁺-doped BiFeO₃ ceramics prepared by a precipitation method. *Ceram. Int.* **2020**, *46*, 25017–25023.
- (10) Turchenko, V.; Kostishin, V. G.; Trukhanov, S.; Damay, F.; Balasoiu, M.; Bozzo, B.; Fina, I.; Burkhevetsky, V. V.; Polosan, S.; Zdrovovets, M.; et al. Structural features, magnetic and ferroelectric properties of SrFe10.8In1.2019 compound. *Mater. Res. Bull.* **2021**, *138*, 111236.
- (11) Trukhanov, S. V.; Zubov, T. I.; Turchenko, V. A.; Matzui, L.; Kmječ, T.; Kohout, J.; Trukhanov, A. V.; Yakovenko, O.; Vinnik, D.; Starikov, A.; et al. Exploration of crystal structure, magnetic and dielectric properties of titanium-barium hexaferrites. *Mater. Sci. Eng., C* **2021**, *272*, 115345.
- (12) Turchenko, V.; Kostishyn, V. G.; Trukhanov, S.; Damay, F.; Porcher, F.; Balasoiu, M.; Lupu, N.; Bozzo, B.; Fina, I.; Trukhanov, A.; et al. Crystal and magnetic structures, magnetic and ferroelectric properties of strontium ferrite partially substituted with in ions. *J. Alloys Compd.* **2020**, *821*, 153412.
- (13) Trukhanov, S. V.; Trukhanov, A. V.; Kostishin, V. G.; Panina, L. V.; Kazakevich, I. S.; Turchenko, V. A.; Oleinik, V. V.; Yakovenko, E. S.; Matsui, L. Y. Magnetic and absorbing properties of M-type substituted hexaferrites BaFe_{12-x}Ga_xO₁₉ (0.1 < x < 1.2). *J. Exp. Theor. Phys.* **2016**, *123*, 461–469.
- (14) Trukhanov, A. V.; Algarou, N. A.; Slimani, Y.; Almessiere, M. A.; Baykal, A.; Tishkevich, D. I.; Vinnik, D. A.; Vakhitov, M. G.; Klygach, D. S.; Silibin, M. V.; et al. Peculiarities of the microwave properties of hard–soft functional composites SrTb_{0.01}Tm_{0.01}Fe_{11.98}O₁₉–AFe₂O₄ (A=Co, Ni, Zn, Cu, or Mn). *RSC Adv.* **2020**, *10*, 32638–32651.
- (15) Yang, Y.; Wang, F.; Shao, J.; Huang, D.; He, H.; Trukhanov, A. V.; Trukhanov, S. V. Influence of Nd–NbZn co-substitution on structural, spectral and magnetic properties of M-type calcium-strontium hexaferrites Ca_{0.4Sr_{0.6}NdxFe_{12.0-x}O₁₉} (Nb_{0.5}Zn_{0.5})_xO₁₉. *J. Alloys Compd.* **2018**, *765*, 616–623.
- (16) Thakur, A.; Sharma, N.; Bhatti, M.; Sharma, M.; Trukhanov, A. V.; Trukhanov, S. V.; Panina, L. V.; Astapovich, K. A.; Thakur, P. Synthesis of barium ferrite nanoparticles using rhizome extract of Acorus calamus: characterization and its efficacy against different plant phytopathogenic fungi. *Nano-Struct. Nano-Objects* **2020**, *24*, 100599.
- (17) Zdrovovets, M. V.; Kozlovskiy, A. L.; Shlimas, D. I.; Borgekov, D. B. Phase transformations in FeCo–Fe₂CoO₄/Co₃O₄–spinel nanostructures as a result of thermal annealing and their practical application. *J. Mater. Sci. Mater. Electron.* **2021**, *32*, 16694–16705.
- (18) Yotburut, B.; Thongbai, P.; Yamwong, T.; Maensiri, S. Synthesis and characterization of multiferroic Sm-doped BiFeO₃ nanopowders and their bulk dielectric properties. *J. Magn. Magn. Mater.* **2017**, *437*, 51–61.
- (19) Tholkappiyan, R.; Vishista, K. Effect of niobium on the optical and magnetic properties of bismuth ferrite (BiFeO₃). *Adv. Sci. Eng. Med.* **2014**, *6*, 311–317.

- (20) Durga Rao, T.; Ranjith, R.; Asthana, S. Enhanced magnetization and improved insulating character in Eu substituted BiFeO₃. *J. Appl. Phys.* **2014**, *115*, 124110.
- (21) Suresh, P.; Babu, P. D.; Srinath, S. Role of (La, Gd) co-doping on the enhanced dielectric and magnetic properties of BiFeO₃ ceramics. *Ceram. Int.* **2016**, *42*, 4176–4184.
- (22) Trukhanov, S. V.; Troyanchuk, I. O.; Trukhanov, A. V.; Fita, I. M.; Vasil'ev, A. N.; Maignan, A.; Szymbczak, H. Magnetic properties of La 0.70 Sr 0.30 MnO 2.85 anion-deficient manganite under hydrostatic pressure. *JETP Lett.* **2006**, *83*, 33–36.
- (23) Kozlovskiy, A.; Egizbek, K.; Zdrovets, M. V.; Ibragimova, M.; Shumskaya, A.; Rogachev, A. A.; Ignatovich, Z. V.; Kadryzhanov, K. Evaluation of the efficiency of detection and capture of manganese in aqueous solutions of FeCeO_x nanocomposites doped with Nb₂O₅. *Sensors* **2020**, *20*, 4851.
- (24) Suresh, P.; Srinath, S. Study of structure and magnetic properties of rare earth doped BiFeO₃. *Phys. B* **2014**, *448*, 281–284.
- (25) Suresh, P.; Babu, P. D.; Srinath, S. Role of (La, Gd) co-doping on the enhanced dielectric and magnetic properties of BiFeO₃ ceramics. *Ceram. Int.* **2016**, *42*, 4176–4184.
- (26) Islam, M. R.; Islam, M. S.; Zubair, M. A.; Usama, H. M.; Azam, M. S.; Sharif, A. Evidence of superparamagnetism and improved electrical properties in Ba and Ta co-doped BiFeO₃ ceramics. *J. Alloys Compd.* **2018**, *735*, 2584–2596.
- (27) Yotburut, B.; Thongbai, P.; Yamwong, T.; Maensiri, S. Electrical and nonlinear current-voltage characteristics of La-doped BiFeO₃ ceramics. *Ceram. Int.* **2017**, *43*, 5616–5627.
- (28) Eerenstein, W.; Mathur, N. D.; Scott, J. F. Multiferroic and magnetoelectric materials. *nature* **2006**, *442*, 759–765.
- (29) Vopson, M. M. Fundamentals of multiferroic materials and their possible applications. *Crit. Rev. Solid State Mater. Sci.* **2015**, *40*, 223–250.
- (30) Catalan, G.; Scott, J. F. Physics and applications of bismuth ferrite. *Adv. Mater.* **2009**, *21*, 2463–2485.
- (31) Wu, J.; Fan, Z.; Xiao, D.; Zhu, J.; Wang, J. Multiferroic bismuth ferrite-based materials for multifunctional applications: Ceramic bulks, thin films and nanostructures. *Prog. Mater. Sci.* **2016**, *84*, 335–402.
- (32) Rojac, T.; Bencan, A.; Malic, B.; Tutuncu, G.; Jones, J. L.; Daniels, J. E.; Damjanovic, D. BiFeO₃ ceramics: processing, electrical, and electromechanical properties. *J. Am. Ceram. Soc.* **2014**, *97*, 1993–2011.
- (33) Valant, M.; Axelsson, A. K.; Alford, N. Peculiarities of a solid-state synthesis of multiferroic polycrystalline BiFeO₃. *Chem. Mater.* **2007**, *19*, 5431–5436.
- (34) Perejon, A.; Sanchez-Jimenez, P. E.; Criado, J. M.; Perez-Maqueza, L. A. Thermal stability of multiferroic BiFeO₃: kinetic nature of the β - γ transition and peritectic decomposition. *J. Phys. Chem. C* **2014**, *118*, 26387–26395.
- (35) Dias, G. S.; Silveira, L. G. D.; Cótica, L. F.; Santos, I. A.; Coelho, A. A.; Garcia, D.; Eiras, J. A.; Sampaio, J. A. Effect of the synthesis atmosphere on the magnetic and structural properties of TbMnO₃ multiferroic polycrystals. *Scripta Mater.* **2014**, *89*, 65–68.
- (36) Micache, A. J.; de Oliveira, O. G.; Silva, R.; Silva, D. M.; Volnistem, E. A.; Dias, G. S.; Santos, I. A.; Guo, R.; Bhalla, A. S.; Cotica, L. F. Synthesis and ferroic and multiferroic studies on Bi_{1-x}NdxFeO₃·0.99CoO_{0.01}O₃ compositions. *Ferroelectrics* **2018**, *534*, 114–120.
- (37) Jiang, Q. H.; Ma, J.; Lin, Y. H.; Nan, C. W.; Shi, Z.; Shen, Z. J. Multiferroic properties of Bi 0.87 La 0.05 Tb 0.08 Fe O 3 ceramics prepared by spark plasma sintering. *Appl. Phys. Lett.* **2007**, *91*, 022914.
- (38) Shannon, R. D. Revised effective ionic radii and systematic studies of interatomic distances in halides and chalcogenides. *Acta Crystallogr., Sect. A: Cryst. Phys., Diffraction, Theor. Gen. Crystallogr.* **1976**, *32*, 751–767.
- (39) Ali, A.; Zaman, A.; Aldulmani, S. A. A.; Abbas, M.; Mushtaq, M.; Bashir, K.; Amami, M.; Althubeiti, K. Structural Evolution and Microwave Dielectric Properties of Ba_{1-x} Sr_x Ti4O₉ (0.0 ≤ x ≤ 0.06). *Ceramics. ACS Omega* **2022**, *7*, 2331–2336.
- (40) Wang, S. Y.; Qiu, X.; Gao, J.; Feng, Y.; Su, W. N.; Zheng, J. X.; Yu, D. S.; Li, D. J. Electrical reliability and leakage mechanisms in highly resistive multiferroic La 0.1 Bi 0.9 FeO 3 ceramics. *Appl. Phys. Lett.* **2011**, *98*, 152902.
- (41) Ali, A.; Jameel, M. H.; Uddin, S.; Zaman, A.; Iqbal, Z.; Gul, Q.; Sultana, F.; Mushtaq, M.; Althubeiti, K.; Ullah, R. The effect of Ca dopant on the electrical and dielectric properties of BaTi4O9 sintered ceramics. *Materials* **2021**, *14*, 5375.
- (42) Saleem, S.; Jameel, M. H.; Akhtar, N.; Nazir, N.; Ali, A.; Zaman, A.; Rehman, A.; Butt, S.; Sultana, F.; Mushtaq, M.; et al. Modification in structural, optical, morphological, and electrical properties of zinc oxide (ZnO) nanoparticles (NPs) by metal (Ni, Co) dopants for electronic device applications. *Arab. J. Chem.* **2022**, *15*, 103518.
- (43) Pillai, S.; Bhuwal, D.; Shripathi, T.; Shelke, V. Synthesis of single phase bismuth ferrite compound by reliable one-step method. *J. Mater. Sci. Mater. Electron.* **2013**, *24*, 2950–2955.
- (44) Chaturvedi, S.; Sarkar, I.; Shirolkar, M. M.; Jeng, U. S.; Yeh, Y. Q.; Rajendra, R.; Ballav, N.; Kulkarni, S. Probing bismuth ferrite nanoparticles by hard x-ray photoemission: Anomalous occurrence of metallic bismuth. *Appl. Phys. Lett.* **2014**, *105*, 102910.
- (45) Moubah, R.; Schmerber, G.; Rousseau, O.; Colson, D.; Viret, M. Photoluminescence investigation of defects and optical band gap in multiferroic BiFeO₃ single crystals. *Appl. Phys. Exp.* **2012**, *5*, 035802.
- (46) Anshul, A.; Kumar, A.; Gupta, B. K.; Kotnala, R. K.; Scott, J. F.; Katiyar, R. S. Photoluminescence and time-resolved spectroscopy in multiferroic BiFeO₃: Effects of electric fields and sample aging. *Appl. Phys. Lett.* **2013**, *102*, 222901.
- (47) Prashanthi, K.; Gupta, M.; Tsui, Y. Y.; Thundat, T. Effect of annealing atmosphere on microstructural and photoluminescence characteristics of multiferroic BiFeO₃ thin films prepared by pulsed laser deposition technique. *Appl. Phys. A: Mater. Sci. Process.* **2013**, *110*, 903–907.
- (48) Basu, S. R.; Martin, L. W.; Chu, Y. H.; Gajek, M.; Ramesh, R.; Rai, R. C.; Xu, X.; Musfeldt, J. L. Photoconductivity in Bi Fe O 3 thin films. *Appl. Phys. Lett.* **2008**, *92*, 091905.
- (49) Chauhan, S.; Kumar, M.; Chhoker, S.; Katyal, S. C.; Singh, H.; Jewariya, M.; Yadav, K. L. Multiferroic, magnetoelectric and optical properties of Mn doped BiFeO₃ nanoparticles. *Solid State Commun.* **2012**, *152*, 525–529.
- (50) Chen, X.; Zhang, H.; Wang, T.; Wang, F.; Shi, W. Optical and photoluminescence properties of BiFeO₃ thin films grown on ITO-coated glass substrates by chemical solution deposition. *Phys. Status Solidi A* **2012**, *209*, 1456–1460.
- (51) Prashanthi, K.; Thakur, G.; Thundat, T. Surface enhanced strong visible photoluminescence from one-dimensional multiferroic BiFeO₃ nanostructures. *Surf. Sci.* **2012**, *606*, L83–L86.
- (52) Miriyala, N.; Prashanthi, K.; Thundat, T. Oxygen vacancy dominant strong visible photoluminescence from BiFeO₃ nanotubes. *Phys. Status Solidi RRL* **2013**, *7*, 668–671.
- (53) Wang, N.; Luo, X.; Han, L.; Zhang, Z.; Zhang, R.; Olin, H.; Yang, Y. Structure, performance, and application of BiFeO₃ nanomaterials. *Nano-Micro Lett.* **2020**, *12*, 81.
- (54) Zhang, Q.; Gong, W.; Wang, J.; Ning, X.; Wang, Z.; Zhao, X.; Ren, W.; Zhang, Z. Size-dependent magnetic, photoabsorbing, and photocatalytic properties of single-crystalline Bi₂Fe₄O₉ semiconductor nanocrystals. *J. Phys. Chem. C* **2011**, *115*, 25241–25246.
- (55) Jianmin, L.; Song, J.; Chen, J.; Yu, S.; Jin, D.; Cheng, J. PVA (Polyvinyl Alcohol)-assisted Hydrothermal Preparation of Bi 25 FeO 40 and Its Photocatalytic Activity. *MRS Online Proc. Libr.* **2009**, *1217*, 322.
- (56) Yan, F.; Zhu, T. J.; Lai, M. O.; Lu, L. Enhanced multiferroic properties and domain structure of La-doped BiFeO₃ thin films. *Scripta Mater.* **2010**, *63*, 780–783.
- (57) Huang, F.; Wang, Z.; Lu, X.; Zhang, J.; Min, K.; Lin, W.; Ti, R.; Xu, T.; He, J.; Yue, C.; et al. Peculiar magnetism of BiFeO₃ nanoparticles with size approaching the period of the spiral spin structure. *Sci. Rep.* **2013**, *3*, 2907.

- (58) Dias, G. S.; Volnistem, E. A.; Leonardo, J. M. P.; Silva, D. M.; Cótica, L. F.; Santos, I. A.; Garcia, D. On the unusual magnetic response of cryomilled BiFeO₃ polycrystals. *Ferroelectrics* **2018**, *534*, 146–151.
- (59) Volnistem, E. A.; Leonardo, J. M.; Silva, V. S.; Silva, D. M.; Dias, G. S.; Cótica, L. F.; Santos, I. A. Tuning the magnetic response of cryo-milled BiFeO₃ nanoparticles by controlling crystallite sizes and internal strain. *Powder Technol.* **2019**, *347*, 215–219.
- (60) Cui, Y. F.; Zhao, Y. G.; Luo, L. B.; Yang, J. J.; Chang, H.; Zhu, M. H.; Xie, D.; Ren, T. L. Dielectric, magnetic, and magnetoelectric properties of La and Ti codoped BiFeO₃. *Appl. Phys. Lett.* **2010**, *97*, 222904.
- (61) Park, T. J.; Papaefthymiou, G. C.; Viescas, A. J.; Moodenbaugh, A. R.; Wong, S. S. Size-dependent magnetic properties of single-crystalline multiferroic BiFeO₃ nanoparticles. *Nano Lett.* **2007**, *7*, 766–772.
- (62) Suresh, P.; Babu, P. D.; Srinath, S. Role of (La, Gd) co-doping on the enhanced dielectric and magnetic properties of BiFeO₃ ceramics. *Ceram. Int.* **2016**, *42*, 4176–4184.
- (63) Yotburut, B.; Thongbai, P.; Yamwong, T.; Maensiri, S. Electrical and nonlinear current-voltage characteristics of La-doped BiFeO₃ ceramics. *Ceram. Int.* **2017**, *43*, 5616–5627.
- (64) Suresh, P.; Srinath, S. Study of structure and magnetic properties of rare earth doped BiFeO₃. *Phys. B* **2014**, *448*, 281–284.